Structural, magnetic and dielectric properties of the novel magnetic spinel compounds $ZnCoSnO_4$ and $ZnCoTiO_4$

Domingo Ruiz-León[1*], Federico Mompean[2], Jesús Prado-Gonjal[2], José F. Marco[3], Mar García-Hernandez[2], Rainer Schmidt[4,5*]

[1] *Departamento de Química de los Materiales, Facultad de Química y Biología, Universidad Santiago de Chile (USACH), Avenida Libertador Bernardo O'Higgins nº 3363, Chile*

[2] *Instituto de Ciencia de Materiales de Madrid ICMM-CSIC, Sor Juana Inés de la Cruz 3, 28049 Madrid, Spain*

[3] *Instituto de Química-Física Rocasolano, CSIC 28006, Madrid, Spain*

[4] *GFMC, Departamento de Física de Materiales, Facultad de Ciencias Físicas, Universidad Complutense de Madrid, 28040 Madrid, Spain*

[5] *Unidad Asociada "Laboratorio de heteroestructuras con aplicación en espintrónica", UCM/CSIC, 28049 Madrid, Spain.*

* Corresponding authors' Email:

domingo.ruiz@usach.cl ; rainerxschmidt@googlemail.com

Abstract

The transparent semiconductor Zn_2SnO_4 with cubic spinel structure and the isostructural Zn_2TiO_4 have been magnetically doped with Co^{2+}. $ZnCoSnO_4$ and $ZnCoTiO_4$ exhibit ferrimagnetism below $T_N \approx 13$ K and $T_N \approx 17$ K. Ferrimagnetic moments are evident in M vs H curves below T_N by small hysteresis. Fits to strictly linear Curie-Weiss plots above T_N give $\mu_{eff} \approx 4.86\ \mu_B$ and $\approx 4.91\ \mu_B$ for $ZnCoSnO_4$ and $ZnCoTiO_4$, above theoretical predictions. Impedance spectroscopy data from sintered ceramic can be fitted with a standard equivalent circuit model based on two RC elements for bulk and GB areas. The relative dielectric permittivity of the bulk is ≈ 20 and ≈ 30 for Zn_2SnO_4 and Zn_2TiO_4. The semiconducting $ZnCoSnO_4$ and $ZnCoTiO_4$ceramics exhibit bulk resistivity of $\approx 1\ 10^6\ \Omega$cm and $\approx 1\ 10^5\ \Omega$cm at 560 K (287 ºC), and bulk activation energies of $E_A \approx 1.2$ eV and 1.1 eV.

I. Introduction

The spinel compound Zn_2SnO_4 is a prominent candidate for applications in dye-sensitized solar cells as a transparent semiconducting electrode [1-4], and in the decomposition of benzene and methylene as a photocatalyst [5-7]. For such applications Zn_2SnO_4 is considered a viable alternative to TiO_2 based materials [8]. Furthermore, the use of spinel Zn_2SnO_4 in Li-ion batteries as an anode material has been demonstrated [9,10]. In the typical spinel structure the O^{2-} anions are cubic closed packed, whereas the cations occupy tetrahedral A-site interstitials by a fraction of 1/3 and octahedral B-sites by 2/3. In Zn_2SnO_4 the Sn^{4+} cations occupy octahedral sites and the Zn^{2+} tetrahedral and octahedral [] sites by equal amounts, i.e. $Zn[ZnSn]O_4$.

In the work presented here, isovalent Co^{2+} magnetic doping of Zn_2SnO_4 and Zn_2TiO_4 by substitution of Zn^{2+} was studied in order to modify the optical absorption properties and increase the functionality of the material by adding a magnetic component to it. The end member spinel compounds Co_2SnO_4 and Co_2TiO_4 exhibit ferrimagnetic moments below T_N = 41 K and T_N = 48 K respectively [11,12], which arise from the different magnetic moments of Co^{2+} on tetrahedral or octahedral sites. From an alternative point of view it may be regarded that the Co^{2+} magnetism in the ferrimagnetic spinels Co_2SnO_4 and Co_2TiO_4 was diluted by partial Zn^{2+} substitution.

Stoichiometric $ZnCoSnO_4$ and $ZnCoTiO_4$ were synthesized by conventional ceramic processing and the structural, microstructural, magnetic and dielectric properties were investigated. Powder X-ray diffraction (XRD) was employed to demonstrate that the O^{2-} sublattice of the spinel structure is ideally suited to accommodate Sn^{4+}, Zn^{2+} and Co^{2+} cations. The valence state of Co was confirmed to be predominantly 2+ in $ZnCoSnO_4$ and $ZnCoTiO_4$ from X-ray photoelectron spectroscopy (XPS) measurements, and the stoichiometry was checked using Energy Dispersive Spectroscopy (EDS).

Magnetic measurement data revealed strictly linear Curie-Weiss fits with Co^{2+} magnetic moments of $\mu_{eff} \approx 4.86\ \mu_B$ and $\approx 4.91\ \mu_B$ for $ZnCoSnO_4$ and $ZnCoTiO_4$, which is significantly above the maximum theoretical prediction of 4.19 μ_B associated with Co^{2+} high spin on octahedral sites. This unusually high Co^{2+} high spin moment may be explained by an exceptionally high orbit contribution or an unusual anisotropy of the *g*-factors $g_{\parallel}$ and $g_{\perp}$. Field cooled and zero field cooled magnetization (*M*) vs temperature (*T*) curves deviate from each other below T_N, typical for a glassy magnetic spin behaviour.

Impedance spectroscopy measurements on $ZnCoSnO_4$ and $ZnCoTiO_4$ pressed and sintered pellets revealed insulating electronic conduction in both compounds. Intrinsic bulk and extrinsic grain boundary (GB) dielectric contributions were detected and analysed separately in terms of the resistivity and dielectric permittivity by fitting the dielectric data to a standard equivalent circuit model containing a series connection of two standard non-ideal RC elements or RQ elements, one each for bulk and GB contributions.

II. Experimental

$ZnCoSnO_4$ and $ZnCoTiO_4$ powders were synthesized using the conventional ceramic method of mixing and homogenizing the analytical grade ZnO (Merck, 99 %), CoO (Merck, 99.9%) and SnO_2 (Merck, 99.9%) precursors in acetone using agate pestle and mortar. The mixed precursor powders were placed in an alumina crucible and calcined in a conventional Labtech LEF-115S muffle furnace for 24 hours at two different temperatures of 900 °C and 1000 °C in two separate sample batches. After calcination, the samples were again ground in an agate mortar and calcined a second time at 900 °C or 1000 °C for 12hr respectively to ensure complete homogeneity. For dielectric measurements the powders were pressed into pellets using a 1 ton uniaxial dye press and sintering of the green ceramic pellets was performed at 1000 °C and

1100 °C for the samples synthesized at 900 °C and 1000 °C respectively, i.e. the sintering temperature was always 100 °C above the synthesis to ensure optimum pellet compaction due to grain growth.

XRD pattern from the synthesized powders were collected at room temperature on a Siemens D5000 powder diffractometer with CuKα radiation at diffraction angles in the range of $5^{o} \leq 2\theta \leq 80^{o}$ with a counting time of 1 s over 0.02° (2θ) steps. The analysis of XRD patterns was performed using the Crystal Impact Match program with the PDF-2 database. The lattice parameters were calculated using the LeBail method in the Fullprof software. XPS spectra were recorded with a CLAM2 electron spectrometer under vacuum below 1 x 10^{-9} mbar, using Mg Kα radiation (1253.6 eV) and a constant pass energy of 200 eV and 20 eV for the wide scan and narrow scan spectra, respectively. All binding energies (BE ± 0.2 eV) were charge–corrected to the C 1s signal of the adventitious contamination carbon layer, set at 284.6eV. The ceramic microstructure of sintered pellets was imaged using a JEOL JSM 6400 scanning electron microscope (SEM). The pellets had been polished, significantly thinned and thermally etched to obtain images representative of the bulk interior microstructure. Energy Dispersive Spectroscopy (EDS) was carried out for quantitative analysis of the stoichiometry using an INCAx-sight detector. The compositional EDS results were confirmed by Inductive-Coupled Plasma (ICP) spectroscopy using an ICP PERKIN ELMER mod. OPTIMA 2100 DV.

A Quantum Design SQUID MPMS was used to measure the powder magnetisation M vs T curves between 5 K and 320 K during heating under ZFC and FC conditions under an applied magnetic field of H = 100 Oe. Furthermore, M vs H curves were measured at 5 K and 15 K below and above the ferrimagnetic transitions T_N to detect possible magnetic hysteresis.

The dielectric properties of the sintered pellets were measured by alternating current (AC) impedance spectroscopy using an Alpha Analyser Novocontrol system. Au electrodes were sputter deposited on both faces of the pellets and covered by Ag conductive paint. Prior to

measurement the short sides of the pellets were polished thoroughly to avoid short-circuiting. Impedance measurements were performed at a frequency (f) range of 1 Hz – 10 MHz with 6 measurement points per frequency decade using an applied AC voltage signal of 0.1 V amplitude under various T between 160 K and 560 K upon heating. The dielectric data were collected in terms of the real and imaginary parts (Z', Z'') of the complex impedance $Z^* = Z' + iZ''$ under steady state conditions, where the selected T was stabilised for ≈ 10 minutes before taking data. Equivalent circuit fitting of the dielectric data was performed by using commercial Z-View software.

III. Results & Discussion

(A) Structural analysis

Figure 1 demonstrates that the XRD patterns of all synthesized $ZnCoSnO_4$ and $ZnCoTiO_4$ powders are strictly single phase and the crystal structure is a cubic spinel in the Fd3m space group. The unit cell parameters were calculated and are listed in Table I. Substitution of the Zn^{2+} cations with an ionic radius of 0.74 Å (VI) in the octahedral or 0.60 Å (IV) in the tetrahedral coordination, by Co^{2+} in the low spin (LS) or high spin (HS) configuration (VI: 0.65 Å LS / 0.75 Å HS; IV: 0.58 Å HS) [13] leads to isostructural phase pure compounds due to the good match of ionic radii.

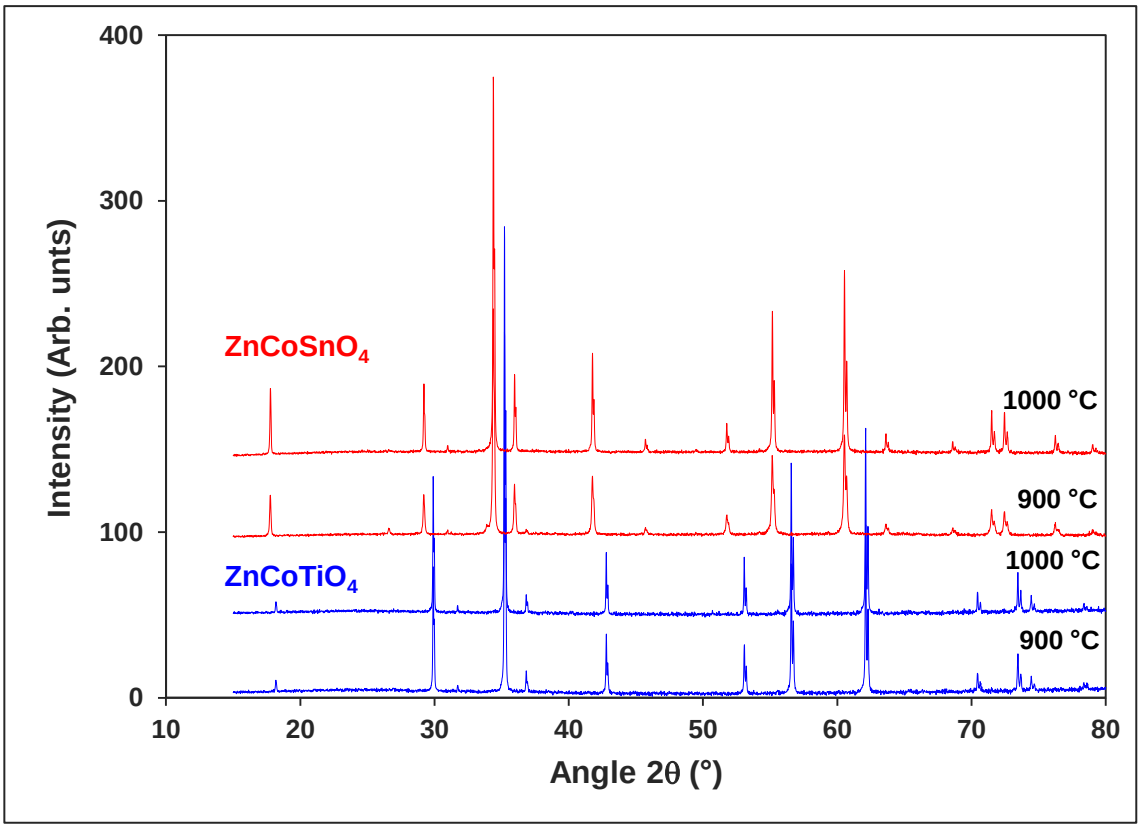

Figure 1. Powder XRD pattern for spinel $ZnCoSnO_4$ and $ZnCoTiO_4$ heat treated at different temperatures. No secondary phases are evident. Large background signals from the fluorescence of Co were subtracted from the data.

Table I. Lattice parameters ***a*** calculated from powder XRD patterns for $ZnCoSnO_4$ and $ZnCoTiO_4$ heat treated at different temperatures.

	$ZnCoSnO_4$		$ZnCoTiO_4$	
	900 °C	1000 °C	900 °C	1000 °C
a (Å)	8.6446(1)	8.6465(1)	8.4457(1)	8.4467(1)

Figures 2 a & b show the wide scan XPS spectra recorded from $ZnCoSnO_4$ and $ZnCoTiO_4$ samples. Only the more intense photoemission lines are labeled. The features of the Co $2p_{3/2}$ line were rather similar for all samples and Figure 2c shows the $ZnCoTiO_4$ Co $2p_{3/2}$ line as a representative example.

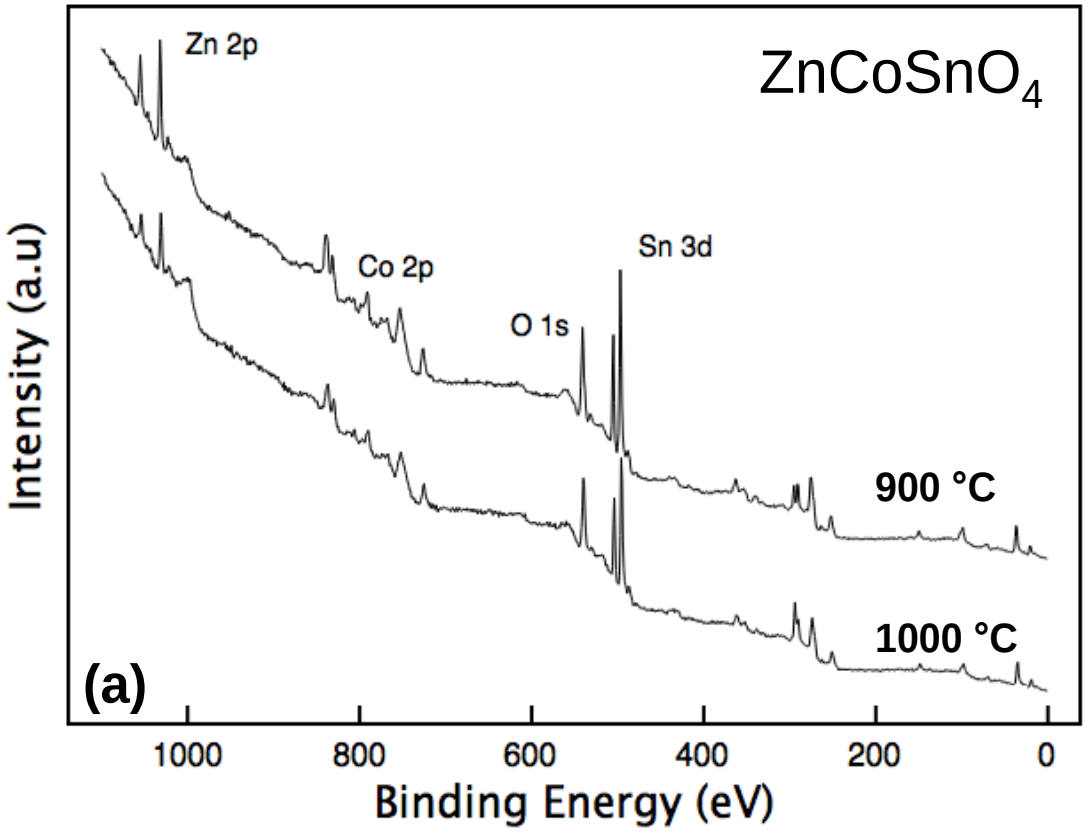
ZnCoSnO4
Zn 2p
Co 2p
O 1s
Sn 3d
900 °C
1000 °C
(a)
Intensity (a.u)
1000
800
600
400
200
0
Binding Energy (eV)

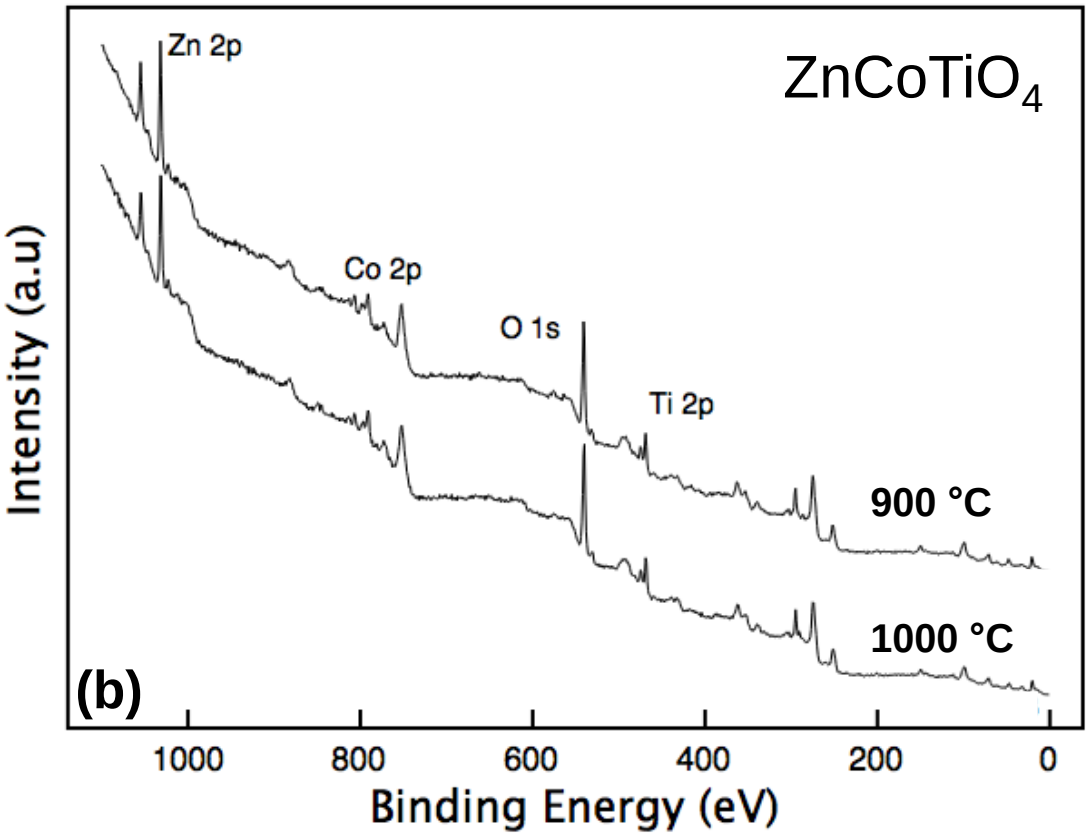
ZnCoTiO4
Zn 2p
Co 2p
O 1s
Ti 2p
900 °C
1000 °C
(b)
Intensity (a.u)
1000
800
600
400
200
0
Binding Energy (eV)

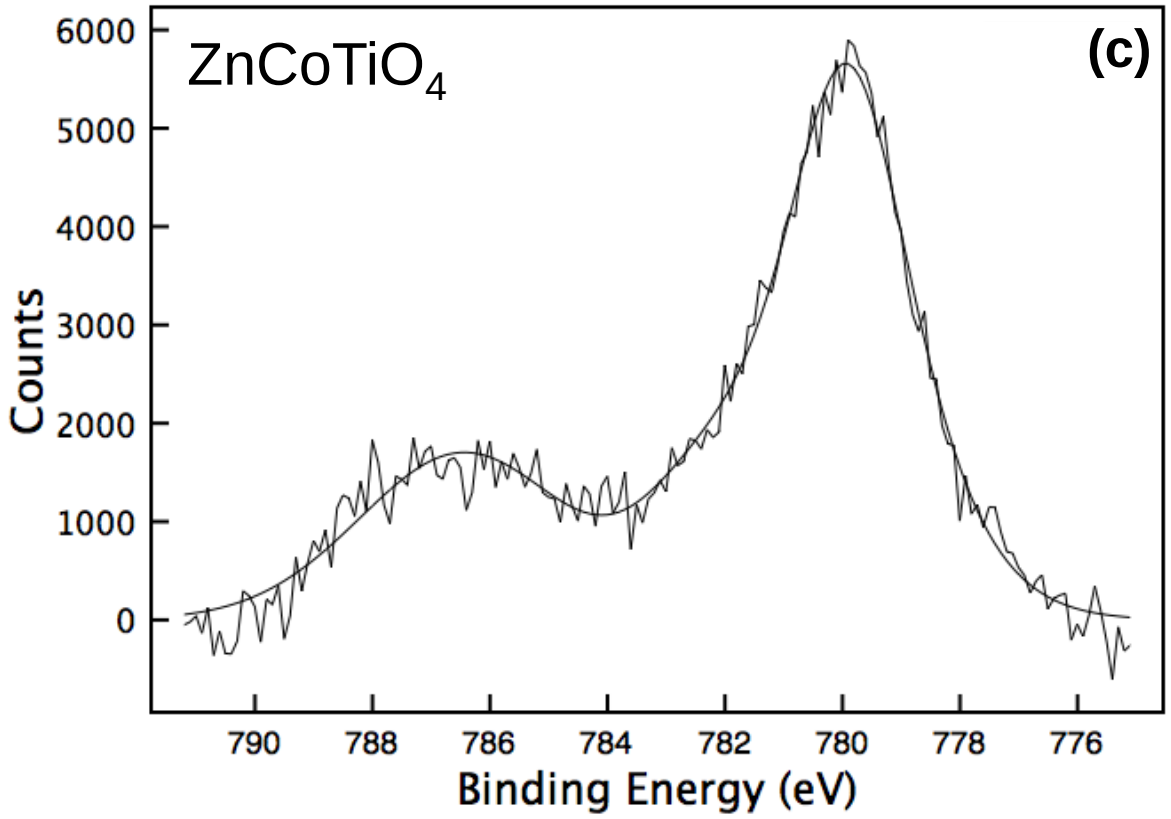

Figure 2. Full XPS spectra for **(a)** $ZnCoSnO_4$ and **(b)** $ZnCoTiO_4$ heat treated at different temperatures. **(c)** Fits to the 2p Co peaks for $ZnCoTiO_4$ treated at 1000 °C. No Co^{3+} traces were detected.

The main photoemission line is centered at 780.1 eV and a strong shake-up satellite at 786. 2 eV is observed. These spectral features and binding energy values are typical for Co^{2+} cations in spinel-related compounds [14]. The existence of some Co^{3+} cations was considered by including the characteristic photoemission line at 779.5 eV into the fits. However, in all cases the quality of the fits did not improve as compared to only Co^{2+} cations and therefore, the presence of considerable amounts of Co^{3+} was discarded. The ceramic microstructure of the bulk interior areas of sintered pellets is demonstrated in Figure 3, where a regular grain structure, and a narrow and uniform grain size distribution were evident in the secondary electron (SE) and backscattered (BE) SEM micrographs.

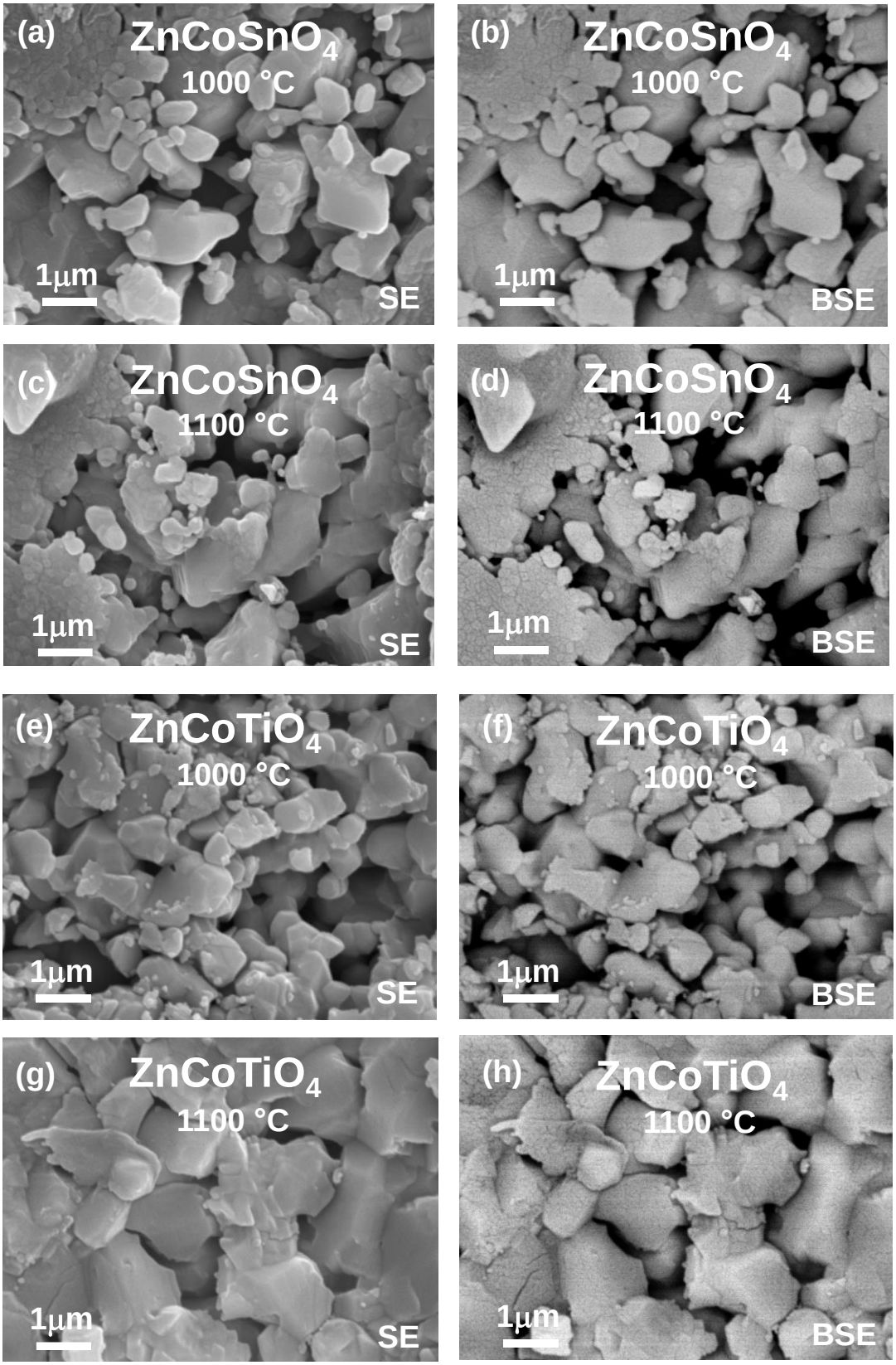

Figure 3. Secondary electron (SE) and backscattered electron (BSE) SEM micrographs for $ZnCoSnO_4$ **(a-d)** and $ZnCoTiO_4$ **(e-h)** ceramic pellets sintered at 1000 ºC and 1100 ºC as indicated.

This indicates that the sintered ceramic pellets may be well-suited for dielectric spectroscopy measurements. The results from quantitative EDS analysis are summarized in Table II. It is indicated that all atomic percentages (at. %) are approximately within the expected range considering the experimental error of EDS analysis of ≈ 2 %.

Table II. Cation ratios in atomic percentage from quantitative analysis by EDS for $ZnCoSnO_4$ and $ZnCoTiO_4$ heat treated at different temperatures. Uncertainties are in the range of ≈ 2%.

	$ZnCoSnO_4$		$ZnCoTiO_4$	
Synthesis Temperature	900 °C	1000 °C	900 °C	1000 °C
Zn (at. %)	31.6(6)	32.5(7)	33.0(7)	32.6(7)
Co (at. %)	32.8(7)	32.4(6)	32.8(7)	33.6(7)
Sn/Ti (at. %)	35.6(7)	35.1(7)	34.2(7)	33.8(7)

(B) Magnetic properties

The *M* vs *T* curves of $ZnCoSnO_4$ and $ZnCoTiO_4$ powder samples heat treated at 1000 °C (Figure 4 a & b) indicate $T_N \approx 13$ and $T_N \approx 17$ respectively. These values are considerably lower as compared to the isostructural compounds Co_2SnO_4 and Co_2TiO_4 (T_N = 41 K and T_N = 48 K), which may well be a result of the diluted Co^{2+} magnetism by Zn^{2+} substitution. Figure 4 further indicates a separation of the ZFC and FC curves below T_N, which is reminiscent of a glassy spin magnetic moment commonly observed in (anti)ferromagnetic and ferrimagnetic spinels [11,15-17]. The Figure 4 insets demonstrate that the deviations between ZFC and FC curves (maxima in the ZFC curves) occur at temperatures very close to the Neel transitions T_N as indicated by the maxima in the differentiated FC curves, for both $ZnCoSnO_4$ and $ZnCoTiO_4$. Therefore, both compounds may enter into a glassy spin state just below T_N, which had been observed previously in Co_2SnO_4 [11,18,19] .

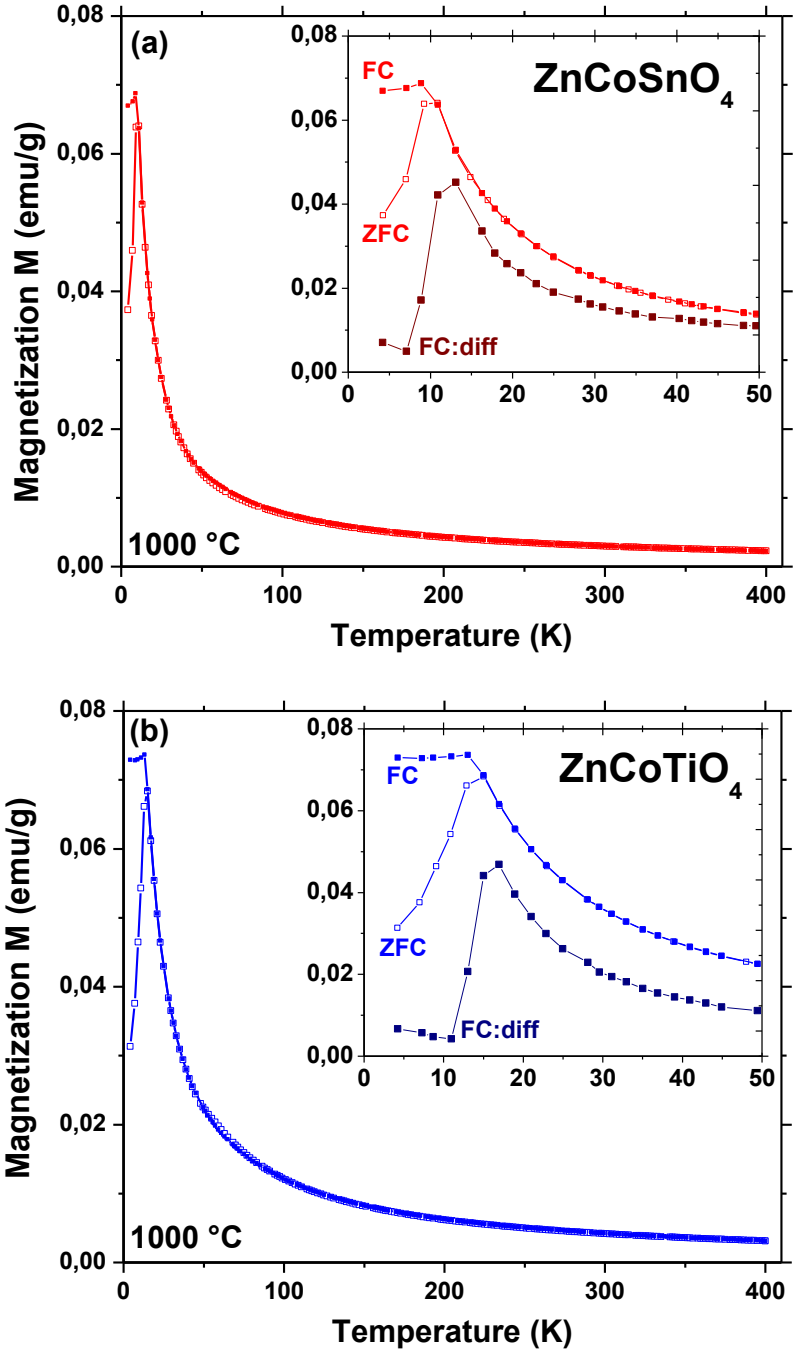

Figure 4. Magnetization *M* (emu/g) vs *T* (K) plots collected under ZFC (open symbols) and FC (filled symbols) conditions for **(a)** $ZnCoSnO_4$ (red symbols) and **(b)** $ZnCoTiO_4$ (blue symbols) powders heat treated at 1000 °C. The figure insets show low *T* magnifications and the differentiated FC curves d*M*/d*T* vs *T* (brown and dark blue symbols). The maxima in the d*M*/d*T* vs *T* curves were regarded the transition temperatures T_N, whereas the peaks in the ZFC curves indicate glassy spin behaviour below T_N.

The magnetic data from $ZnCoSnO_4$ and $ZnCoTiO_4$ powders heat treated at 1100 °C show the equivalent T_N transition temperatures, glassy spin behaviour and ferrimagnetism (data not shown). Therefore, it can be concluded that the magnetism in $ZnCoSnO_4$ and $ZnCoTiO_4$ powders is not affected qualitatively by the differences in heat treatment. The ferrimagnetic moments were confirmed from the hysteretic M vs H curves at T = 4.2 K below T_N, whereas above T_N at 20 K and 40 K approximately linear behaviour is indicated in Figure 5 a & b. The ferrimagnetic moment arises from the different magnetic moments of the Co^{2+} cations situated at tetrahedral or octahedral sites, since the octahedral coordination entails orbit contributions, which are absent in the tetrahedral coordination [20]. This ferrimagnetic moment detected here had been demonstrated previously in the end member compounds Co_2SnO_4 and Co_2TiO_4 [11,12].

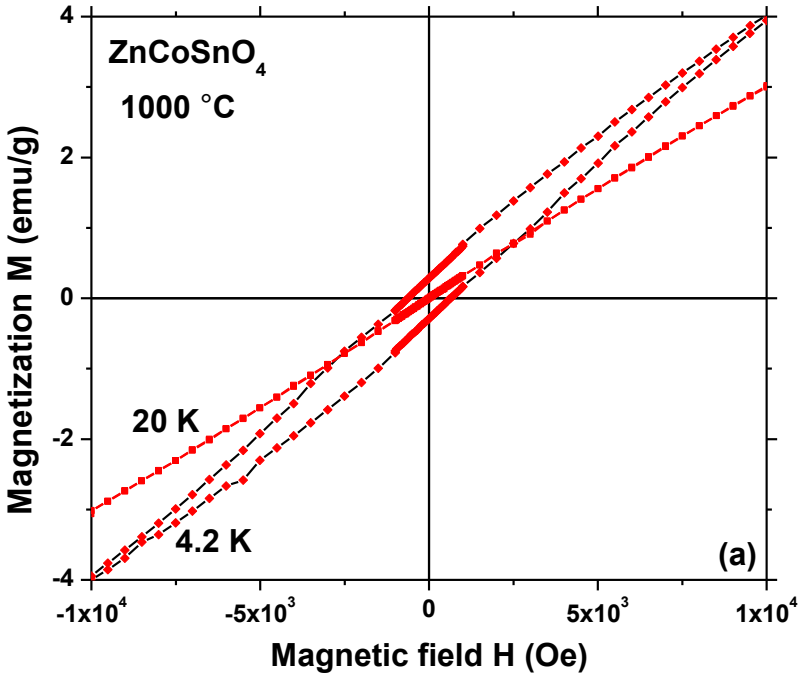

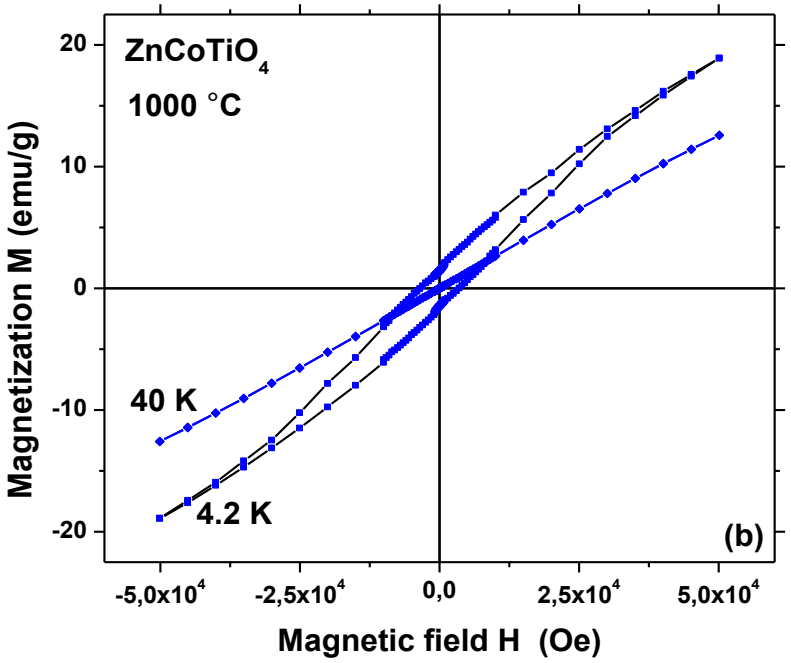

Figure 5. Magnetization *M* (emu/g) vs applied magnetic field *H* (Oe) plots for **(a)** $ZnCoSnO_4$ and **(b)** $ZnCoTiO_4$ powders heat treated at 1000 °C. Small hysteresis loops for $T < T_N$ indicate net ferrimagnetic moments.

The magnetic behaviour of both $ZnCoSnO_4$ and $ZnCoTiO_4$ above T_N in the paramagnetic regime is dominated by strictly linear susceptibility $1/\chi$ vs *T* Curie-Weiss plots, which indicate a conventional paramagnetism of non-interacting magnetic spin moments. However, the linear fits to the Curie-Weiss plots and calculating the total effective magnetic moment μ_{eff} leads to values in the range of $\approx 4.9\ \mu_B$ that are significantly above the maximum values predicted. This is the case even by assuming an HS scenario and full octahedral occupation of Co^{2+} cations with the higher predicted HS moment of 4.16 μ_B as compared to the predicted tetrahedral HS moment of 3.88 μ_B. All μ_{eff} values calculated from the strictly linear Curie-Weiss plots shown in Figure 6 are summarized in Table III. The theoretical predictions for the total μ_{eff} values were calculated assuming a spin-only moment of the tetrahedral Co^{2+} cations, but both spin and orbit contributions for the octahedral Co^{2+} cations in the HS state. The possibility of a mixed

LS/IS/HS spin-state scenario on octahedral Co^{3+} lattice sites has been proposed previously in $LaCoO_3$ perovskites (here in the Co^{2+} spinel only LS/HS mixing on octahedral sites would be possible) [21-26], but this scenario was discarded in this study due to the high μ_{eff} values encountered.

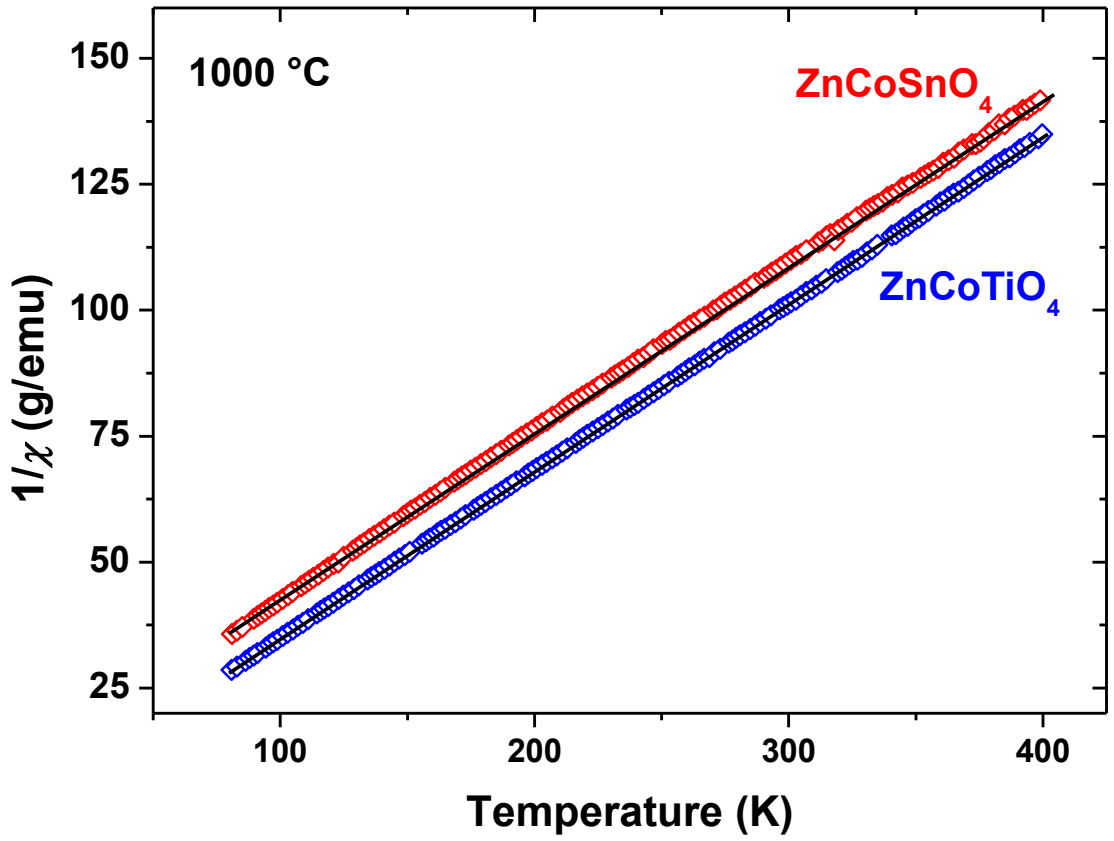

Figure 6. Curie-Weiss plots of $1/\chi$ vs T for $ZnCoSnO_4$ and $ZnCoTiO_4$ powders heat treated at 1000 °C. Both curves show excellent linearity.

Table III. Total efficient magnetic moment μ_{eff} for $ZnCoSnO_4$ and $ZnCoTiO_4$ heat treated at different temperatures. Uncertainties are below 1%.

	$ZnCoSnO_4$		$ZnCoTiO_4$	
Synthesis Temperature	900 °C	1000 °C	900 °C	1000 °C
μ_{eff} (μ_B)	4.91(1)	4.91(1)	4.73(1)	4.91(1)

The detection of an increased magnetic moment in Co^{2+} magnetic cations may be interpreted in terms of an unusually high orbit contribution and strong spin-orbit coupling. However, the detected moment of $\mu_{eff} \approx 4.9\ \mu_B$ is considerably higher than the predicted 4.16 μ_B for a strictly octahedral occupation of Co^{2+}, which in fact may be unrealistic. Due to a close match of the ionic radii on octahedral (Zn^{2+}: 0.74 Å; Co^{2+} HS: 0.75 Å) and tetrahedral (Zn^{2+}: 0.60 Å; Co^{2+} HS: 0.58 Å) sites, a good dispersion of Zn^{2+} and Co^{2+} on tetrahedral and octahedral sites is likely, which would imply an inversion parameter of the spinel structure near $\nu \approx 0.5$. In this case the detected total μ_{eff} would be ≈ 20% above theoretical predictions. It may be doubtful if this large increase can be explained by unusual orbit contributions only, and the alternative explanation of an unusual anisotropy of the *g*-factors $g_{\parallel}$ and $g_{\perp}$ may be considered as well [20]. A possible Co^{2+} excess in the samples could be discarded from the EDS results presented in Table II. Furthermore, ICP spectroscopy data did not give any indications for Co^{2+} excess either.

(C) Dielectric properties

Impedance spectroscopy data from $ZnCoSnO_4$ and $ZnCoTiO_4$ ceramic pellets sintered at 1000 °C and 1100 °C are presented in Figure 7 in form of the complex impedance plots of *Z*'' vs *Z*'. The characteristic semicircles indicate different dielectric contributions, where the data from 1100 °C treated $ZnCoSnO_4$ ceramics (Figure 7b) shows the signs of two strongly overlapping semicircles, whereas the data from the 1100 °C sample indicate electronic homogeneity. On the other hand, the $ZnCoTiO_4$ ceramics sintered at 1000 °C and 1100 °C both show the clear signs of two dielectric contributions (Figure 7 c & d), which can be clearly assigned to intrinsic bulk and grain boundary (GB) [27,28].

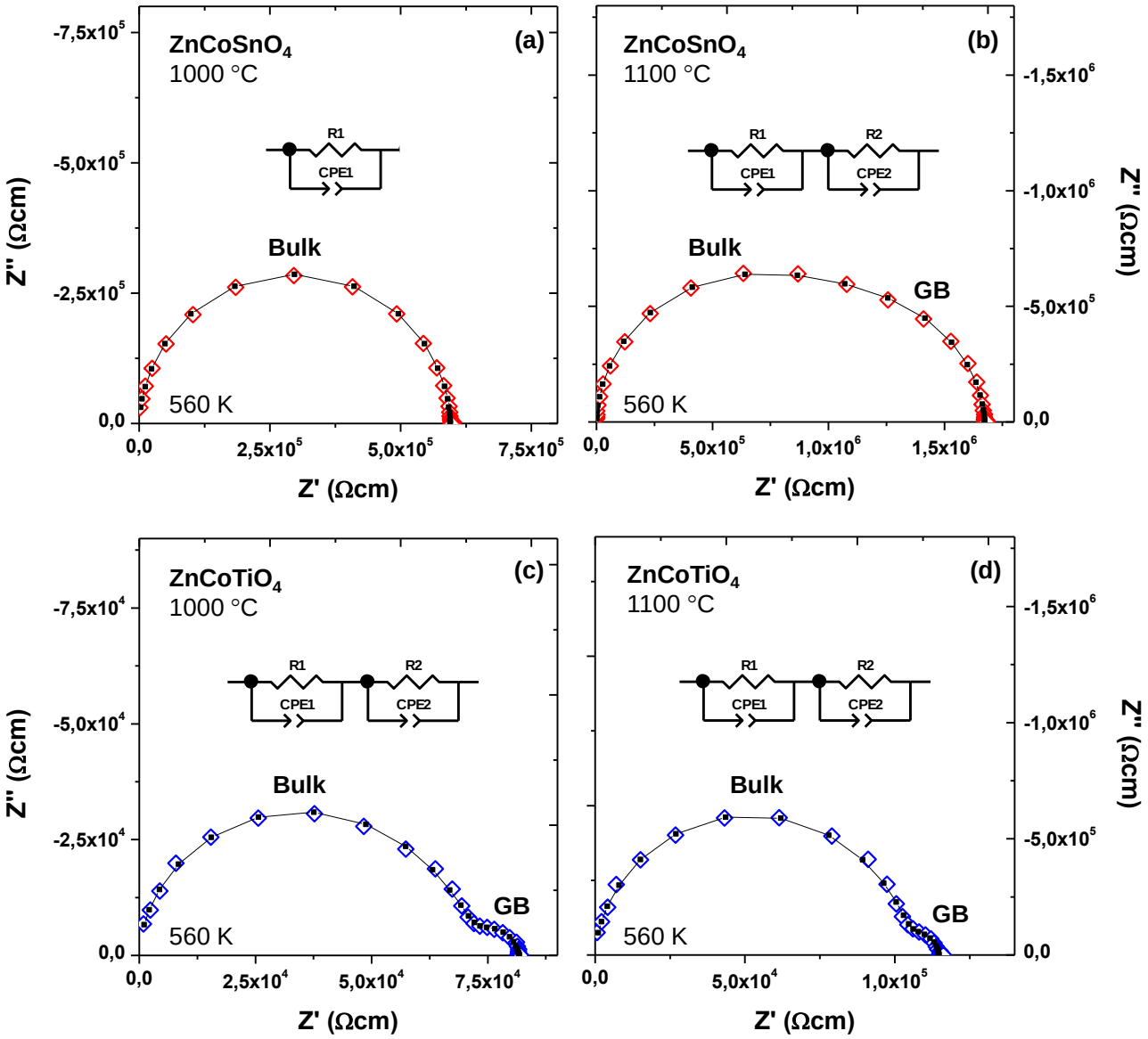

Figure 7. Complex impedance plane plots of Z'' vs Z' for ceramic $ZnCoSnO_4$ sintered at **(a)** 1000 °C and **(b)** 1100 °C, and $ZnCoTiO_4$ sintered at **(c)** 1000 °C and **(d)** 1100 °C. Open symbols correspond to the data, solid squares and lines to the equivalent circuit fits. The circuit models are displayed in the panels. Excellent fits and bulk and GB dielectric contributions are evident.

It is interesting to note that increasing the sintering temperature in $ZnCoSnO_4$ ceramics does not improve the sample's homogeneity but leads to the formation of a dielectrically distinct GB contribution. This points towards a certain degree of chemical inhomogeneity, which may arise within the $ZnCoSnO_4$ ceramics at higher sintering temperatures when the diffusivity of the

constituting atoms increases. Although this behaviour may be reminiscent of the formation of GB barrier layers in dielectric ceramics [29,30], the diameter of the GB semicircle in the1100 °C sintered $ZnCoSnO_4$ ceramic is smaller as compared to the bulk and thus, the barrier effect may not be relevant for potential applications. The dielectric data presented in Figure 7 were fitted to a standard equivalent circuit model containing RC elements of ideal resistors and parallel non-ideal capacitors represented by Constant-Phase element (CPEs), i.e. R-CPE or RQ elements. In the case of two R-CPE elements, they were connected in series to obtain a valid fit and the resistance and capacitance of bulk and GB contributions were extracted [31]. Figure 7 indicates a good fit, which was reflected in low fitting errors (< 5%). The bulk and GB resistance and capacitance values extracted from the fits were normalized by the pellet geometry and plotted in form of the electrical resistivity ρ vs $1/T$ (Figure 8) and the relative dielectric permittivity ε vs T (Figure 9), both on semi-logarithmic axes. The charge transport activation energies E_A (eV), the ε values and the resistivity obtained at 560 K are summarized in Table IV. The resistivity ρ vs $1/T$ plots in Figure 8 show good linearity for $ZnCoSnO_4$ and $ZnCoTiO_4$ ceramics sintered at 1100 °C, which indicates a conventional thermally activated electron charge transport. The E_A values are indicated in Figure 8 and summarized in Table IV.

All E_A values are relatively large for electronic charge transport, but none of the typical signs of ionic charge transport were detected and the charge carriers may well be electrons. The E_A values for the GB contributions are slightly higher, which indicates a lower concentration of charge carriers within the GB areas. Nevertheless, the nominal values of the GB resistance or resistivity are smaller as compared to the bulk values, which is evidenced in Figure 7 and 8 by the size of the respective semicircles and the resistance or resistivity values extracted. This can be understood by a geometrical effect of reduced thickness of the GB areas as compared to the bulk leading to lower resistance, whereas the effective resistivity within the GB areas may in fact be larger than in the bulk.

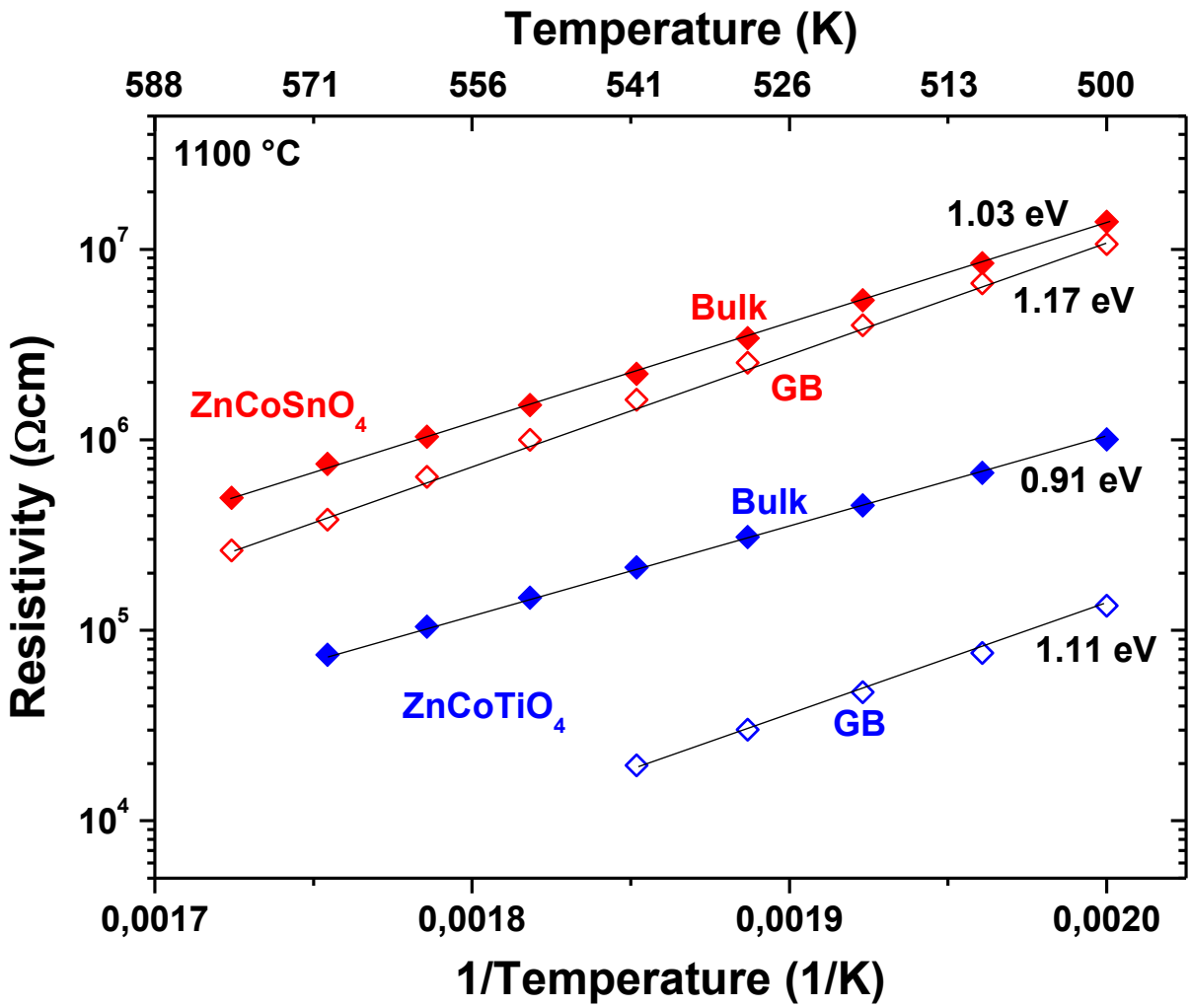

Figure 8. Resistivity vs 1/*T* for bulk and GB dielectric contributions obtained from equivalent circuit fits for ceramic $ZnCoSnO_4$ and $ZnCoTiO_4$ sintered at 1100 °C. Good linearity indicates thermally activated electron transport. The displayed activation energies E_A (eV) were obtained from the respective Arrhenius plots.

All data in Figures 7 & 8 were normalized to the same macroscopic pellet geometry to obtain the resistivity, which may not be adequate for the microscopically thin GB areas and the effective resistivity within GB areas may thus be significantly higher than the bulk, i.e. charge transport can be assumed to be hindered by the GBs. Figure 9 indicates an intrinsic bulk $\varepsilon \approx 20$ and ≈ 30 for $ZnCoSnO_4$ and $ZnCoTiO_4$ ceramics sintered at 1100 °C, respectively.

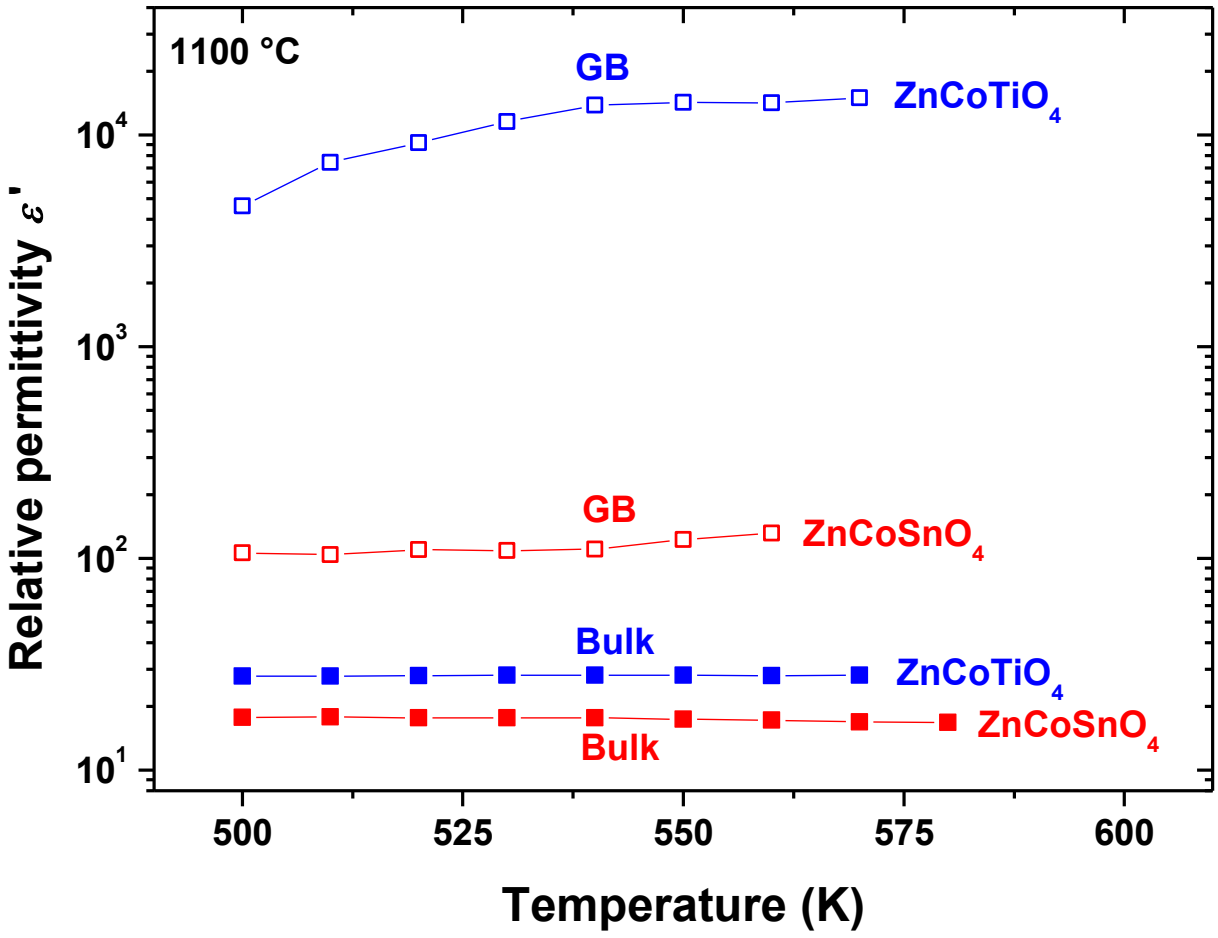

Figure 9. Relative dielectric permittivity vs *T* for bulk and GB dielectric contributions obtained from equivalent circuit fits for ceramic $ZnCoSnO_4$ and $ZnCoTiO_4$ sintered at 1100 °C.

The relative dielectric permittivity values for the 1000 °C sintered pellets are marginally higher in both cases. All ε values are relatively low, especially for $ZnCoTiO_4$. Quite often, Ti^{4+} on octahedral sites leads to larger permittivity values in complex oxides, e.g. ≈ 100 in $CaCu_3Ti_4O_{12}$ [29] and TiO_2 [32], or even to ferroelectricity, e.g. in $BaTiO_3$ [33] and $PbTiO_3$ [34]. It can be concluded that $ZnCoSnO_4$ and $ZnCoTiO_4$ exhibit a dielectric permittivity that is typical for standard dielectric materials. The GB permittivity is higher than the bulk permittivity by a factor of ≈ 5

- 10 and ≈ 300 for $ZnCoSnO_4$ and $ZnCoTiO_4$ ceramics, respectively. Both values are in a typical range for extrinsic GB contributions [35].

Table IV. Bulk and GB resistivity ρ, activation energy E_A and dielectric permittivity ε for $ZnCoSnO_4$ and $ZnCoTiO_4$ ceramics sintered at different temperatures.

	$ZnCoSnO_4$		$ZnCoTiO_4$	
Sintering Temperature	1000 °C	1100 °C	1000 °C	1100 °C
ρ (560 K) Bulk (Ωcm)	$5.96\ 10^5 \pm 4\ 10^2$	$1.04\ 10^6 \pm 3\ 10^4$	$7.05\ 10^4 \pm 3\ 10^2$	$1.04\ 10^5 \pm 4\ 10^2$
ρ (560 K) GB (Ωcm)	--	$6.39\ 10^5 \pm 3\ 10^4$	$1.11\ 10^4 \pm 3\ 10^2$	$1.05\ 10^4 \pm 4\ 10^2$
E_A Bulk (eV)	1.085(1)	1.032(8)	0.915(5)	0.915(3)
E_A GB (eV)	--	1.17(2)	1.04(2)	1.11(2)
ε Bulk	22.8(1)	17.4(4)	31.3(1)	28.0(1)
ε GB	--	≈ 120 ± 20	≈ 10000 ± 2000	≈ 10000 ± 4000

IV. Conclusions

The compounds $ZnCoSnO_4$ and $ZnCoTiO_4$ have been synthesized successfully and characterized comprehensively. Both compounds crystallize in a cubic spinel structure and exhibit ferrimagnetism below T_N. The Co^{2+} spin states were suggested to be HS in both compounds above theoretical predictions. Electronic conduction was detected at elevated temperature and $ZnCoSnO_4$ and $ZnCoTiO_4$ may be regarded bad electronic insulators or high resistivity semiconductors. This work demonstrates that transparent semiconductors like Zn_2SnO_4 can be doped magnetically to increase their functionality.

Acknowledgments

R.S. acknowledges a travel grant (Convenio Internacional) from the Universidad Complutense de Madrid to visit the USACH in Chile. JPG thanks the Spanish MINECO for granting a Juan de la Cierva fellowship. Spanish MINECO grant MAT2014-52405-C2-2-R is also acknowledged.

References

(1) Lana-Villarreal, T.; Boschloo, G.; Hagfeldt, A. Nanostructured Zinc Stannate as Semiconductor Working Electrodes for Dye-Sensitized Solar Cells. *The Journal of Physical Chemistry C* **2007,** *111* (14), 5549.

(2) Tan, B.; Toman, E.; Li, Y.; Wu, Y. Zinc Stannate (Zn_2SnO_4) Dye-Sensitized Solar Cells. *Journal of the American Chemical Society* **2007,** *129* (14), 4162.

(3) Shin, S. S.; Yang, W. S.; Noh, J. H.; Suk, J. H.; Jeon, N. J.; Park, J. H.; Kim, J. S.; Seong, W. M.; Seok, S. I. High-performance flexible perovskite solar cells exploiting Zn_2SnO_4 prepared in solution below 100 °C. *Nature Communications* **2015,** *6*, 7410.

(4) Li, Z.; Zhou, Y.; Zhang, J.; Tu, W.; Liu, Q.; Yu, T.; Zou, Z. Hexagonal Nanoplate-Textured Micro-Octahedron Zn_2SnO_4: Combined Effects toward Enhanced Efficiencies of Dye-Sensitized Solar Cell and Photoreduction of CO2 into Hydrocarbon Fuels. *Crystal Growth & Design* **2012,** *12* (3), 1476.

(5) Alpuche-Aviles, M. A.; Wu, Y. Photoelectrochemical Study of the Band Structure of Zn_2SnO_4 Prepared by the Hydrothermal Method. *Journal of the American Chemical Society* **2009,** *131* (9), 3216.

(6) Govindappa, C. K.; Venkatarangaiah, V. T.; Hamid, S. B. A. Electrochemical Generation of Cubic Shaped Nano Zn_2SnO_4 Photocatalysts. *Nano-Micro Letters* **2013,** *5* (2), 101.

(7) Cun, W.; Xinming, W.; Jincai, Z.; Bixian, M.; Guoying, S.; Ping'an, P.; Jiamo, F. Synthesis, characterization and photocatalytic property of nano-sized Zn_2SnO_4. *Journal of Materials Science* **2002,** *37* (14), 2989.

(8) Ruiz-León, D.; Avila, R. E.; Venegas, C. J. Synthesis and electrical characterization of zinc stannate (zto) prepared by hydrothermal method. *Journal of the Chilenian Chemical Society* **2015,** *60* (3), 3029.

(9) Zhu, X. J.; Geng, L. M.; Zhang, F. Q.; Liu, Y. X.; Cheng, L. B. Synthesis and performance of Zn_2SnO_4 as anode materials for lithium ion batteries by hydrothermal method. *Journal of Power Sources* **2009,** *189* (1), 828.

(10) Yuan, W. S.; Tian, Y. W.; Liu, G. Q. Synthesis and electrochemical properties of pure phase Zn_2SnO_4 and composite Zn_2SnO_4/C. *Journal of Alloys and Compounds* **2010,** *506* (2), 683.

(11) Nayak, S.; Dasari, K.; Joshi, D. C.; Pramanik, P.; Palai, R.; Waske, A.; Chauhan, R. N.; Tiwari, N.; Sarkar, T.; Thota, S. Low-temperature anomalous magnetic behavior of Co_2TiO_4 and Co_2SnO_4. *Journal of Applied Physics* **2016,** *120* (16), 163905.

(12) Nayak, S.; Thota, S.; Joshi, D. C.; Krautz, M.; Waske, A.; Behler, A.; Eckert, J.; Sarkar, T.; Andersson, M. S.; Mathieu, R.et al. Magnetic compensation, field-dependent magnetization reversal, and complex magnetic ordering in $CoTiO_4$. *Physical Review B* **2015,** *92* (21), 214434.
(13) Shannon, R. D. Revised Effective Ionic Radii and Systematic Studies of Interatomic Distances in Halides and Chalcogenides. *Acta Crystallographica A* **1976,** *32*, 751.
(14) Marco, J. F.; Gancedo, J. R.; Ortiz, J.; Gautier, J. L. Characterization of the spinel-related oxides $Ni_xCo_{3-x}O_4$ (x=0.3,1.3,1.8) prepared by spray pyrolysis at 350 °C. *Applied Surface Science* **2004,** *227* (1), 175.
(15) Fiorani, D.; Viticoli, S.; Dormann, J. L.; Tholence, J. L.; Murani, A. P. Spin-glass behavior in an antiferromagnetic frustrated spinel: $ZnCr_{1.6}Ga_{0.4}O_4$. *Physical Review B* **1984,** *30* (5), 2776.
(16) Jang, Y. I.; Chou, F. C.; Chiang, Y. M. Spin-glass behavior in $LiMn_2O_4$ spinel. *Applied Physics Letters* **1999,** *74* (17), 2504.
(17) Poole, C. P.; Farach, H. A. Magnetic phase diagram of spinel spin-glasses. *Zeitschrift für Physik B Condensed Matter* **1982,** *47* (1), 55.
(18) Thota, S.; Narang, V.; Nayak, S.; Sambasivam, S.; Choi, B. C.; Sarkar, T.; Andersson, M. S.; Mathieu, R.; Seehra, M. S. On the nature of magnetic state in the spinel Co_2SnO_4. *Journal of Physics: Condensed Matter* **2015,** *27* (16), 166001.
(19) Thota, S.; Seehra, M. S. Co-existence of ferrimagnetism and spin-glass state in the spinel Co_2SnO_4. *Journal of Applied Physics* **2013,** *113* (20), 203905.
(20) Carlin, R. L.; van Duyneveldt, A. J. *Magnetic Properties of Transition Metal Compounds*; Springer-Verlag: New York Heidelberg Berlin, 1977.
(21) Kozlenko, D. P.; Golosova, N. O.; Jirak, Z.; Dubrovinsky, L. S.; Savenko, B. N.; Tucker, M. G.; Godec, Y. L.; Glazkov, V. P. Temperature- and pressure-driven spin-state transitions in $LaCoO_3$. *Physical Review B* **2007,** *75* (6), 064422.
(22) Schmidt, R.; Wu, J.; Leighton, C.; Terry, I. Dielectric response to the low-temperature magnetic defect structure and spin state transition in polycrystalline $LaCoO_3$. *Physical Review B* **2009,** *79*, 125105.
(23) Prado-Gonjal, J.; Gutiérrez-Seijas, J.; Ansorregui, I. H.; Morán, E.; Terry, I.; Schmidt, R. The role of defects in microwave and conventionally synthesized LaCoO3 perovskite. *Journal of the European Ceramic Society* **2016,** *36* (5), 1197.
(24) Nagaev, E. L.; Podelshchikov, A. I. Phase separation and resistivity jumps in Co compounds and other materials with low-spin-high-spin transitions. *Journal of Physics-Condensed Matter* **1996,** *8* (30), 5611.
(25) Gutiérrez Seijas, J.; Prado-Gonjal, J.; Ávila Brande, D.; Terry, I.; Morán, E.; Schmidt, R. Microwave-Assisted Synthesis, Microstructure, and Magnetic Properties of Rare-Earth Cobaltites. *Inorganic Chemistry* **2017,** *56* (1), 627.
(26) Haverkort, M. W.; Hu, Z.; Cezar, J. C.; Burnus, T.; Hartmann, H.; Reuther, M.; Zobel, C.; Lorenz, T.; Tanaka, A.; Brookes, N. B.et al. Spin State Transition in $LaCoO_3$ Studied Using Soft X-ray Absorption Spectroscopy and Magnetic Circular Dichroism. *Physical Review Letters* **2006,** *97* (17), 176405.
(27) Barsukov, E.; Macdonald, J. *Impedance Spectroscopy: Theory, Experiment and Applications*; John Wiley & Sons Inc.: Hoboken, 2005.
(28) Schmidt, R. In *Ceramic Materials Research Trends*; Lin, P. B., Ed.; Novascience Publishers: Hauppauge, 2007.
(29) Adams, T. B.; Sinclair, D. C.; West, A. R. Giant Barrier Layer Capacitance Effects in $CaCu_3Ti_4O_{12}$ Ceramics. *Advanced Materials* **2002,** *14* (18), 1321.
(30) Schmidt, R.; Stennett, M. C.; Hyatt, N. C.; Pokorny, J.; Prado-Gonjal, J.; Li, M.; Sinclair, D. C. Effects of sintering temperature on the internal barrier layer capacitor

(IBLC) structure in $CaCu_3Ti_4O_{12}$ (CCTO) ceramics. *Journal of the European Ceramic Society* **2012,** *32* (12), 3313.

(31) Schmidt, R. In *CRC Concise Encyclopedia of Nanotechnology*; Kharisov, B.;Kharissova, O.;Ortiz-Mendez, U., Eds.; CRC Press Taylor & Francis Group: Boca Raton (USA), 2015.

(32) Wypych, A.; Bobowska, I.; Tracz, M.; Opasinska, A.; Kadlubowski, S.; Krzywania-Kaliszewska, A.; Grobelny, J.; Wojciechowski, P. Dielectric Properties and Characterisation of Titanium Dioxide Obtained by Different Chemistry Methods. *Journal of Nanomaterials* **2014,** *2014*, 9.

(33) Morrison, F. D.; Sinclair, D. C.; West, A. R. Electrical and structural characteristics of lanthanum-doped barium titanate ceramics. *Journal of Applied Physics* **1999,** *86* (11), 6355.

(34) Randall, C. A.; Eitel, R.; Jones, B.; Shrout, T. R.; Woodward, D. I.; Reaney, I. M. Investigation of a high Tc piezoelectric system: $(1-x)Bi(Mg_{1/2}Ti_{1/2})O_3–(x)PbTiO_3$. *Journal of Applied Physics* **2004,** *95* (7), 3633.

(35) Irvine, J. T. S.; Sinclair, D. C.; West, A. R. Electroceramics: Characterization by Impedance Spectroscopy. *Advanced Materials* **1990,** *2* (3), 132.